Absorption spectroscopy of the rubidium dimer in an overheated vapor: An accurate check of molecular structure and dynamics

R. Beuc,[1] M. Movre,[1] V. Horvatic,[1,*] C. Vadla,[1] O. Dulieu,[2] and M. Aymar[2]

[1]*Institute of Physics, Bijenicka 46, 10000 Zagreb, Croatia*
[2]*Laboratoire Aimé Cotton, CNRS, Campus d'Orsay, 91405 Orsay Cedex, France*

Experimental studies of the absorption spectrum of the Rb$_2$ dimer are performed in the 600–1100 nm wavelength range for temperatures between 615 and 745 K. The reduced absorption coefficient is measured by spatially resolved white light absorption in overheated rubidium vapor with a radial temperature gradient, which enables simultaneous measurements at different temperatures. Semiclassical and quantum spectral simulations are obtained by taking into account all possible transitions involving the potential curves stemming from the 5 ^2S+5 ^2S and 5 ^2S+5 ^2P asymptotes. The most accurate experimental potential curves are used where available, and newly calculated potential curves and transition dipole moments otherwise. The overall consistency of the theoretical model with the experimental interpretation is obtained only if the radial dependence of both the calculated transition dipole moments and the spin-orbit coupling is taken into account. This highlights the low-resolution absorption spectroscopy as a valuable tool for checking the accuracy of molecular electronic structure calculations.

PACS number(s): 31.15.Gy, 33.20.Ea, 33.20.Kf, 33.70.Fd

I. INTRODUCTION

There is a renewed interest in the theoretical and experimental investigation of the absorption spectra of alkali-metal dimers at elevated temperatures. Recently, theoretical studies of Li$_2$ [1] and Na$_2$ [2] molecular bands at temperatures of the order of 1000 K have been published. Experimental and theoretical studies of the temperature dependence of the most pronounced atomic, molecular, and diffuse features appearing in the K$_2$ spectrum have been reported in the range between 650 and 1100 K [3]. Motivations for such investigations include the improvement of molecular data resulting from quantum chemistry calculations, spectroscopy, ultracold atom, and molecule studies, as well as the prediction of spectra at temperatures relevant to high-pressure alkali-metal lamps [2], or the determination of atom number densities in dense alkali-metal vapors [3].

In the present paper the investigation of alkali-metal dimer absorption spectra is extended to rubidium dimer, whose spectroscopy is only partially known up to now, even for low excited states. Semiclassical and quantum mechanical simulations of the prominent spectral features of the Rb$_2$ dimer in the wavelength range of 600–1100 nm at temperatures between 615 and 745 K are accompanied with, and compared to the measurements of the reduced absorption coefficient in an overheated rubidium vapor.

The investigated molecular bands are related to the transitions between the Rb($5S$)+Rb($5S$) and Rb($5S$)+Rb($5P$) interaction potentials (see Fig. 1). Throughout the paper the states of given symmetry conforming to the standard $^{2S+1}\Lambda_{g/u}^{+/-}$ Hund's case-(a) notation are labeled in order of increasing energy. Where appropriate, we will also use traditional spectroscopic indexes X, A, B, b, etc. The most pronounced spectral features on which we will focus in the following are the well-known *X-A* and *X-B* molecular bands, which emerge in the singlet transitions 1 $^1\Sigma_g^+ \to 1$ $^1\Sigma_u^+$ and 1 $^1\Sigma_g^+ \to 1$ $^1\Pi_u$, respectively (or X $^1\Sigma_g^+ \to A$ $^1\Sigma_u^+$ and X $^1\Sigma_g^+ \to B$ $^1\Pi_u$).

The entire ground state potential 1 $^1\Sigma_g^+$ is accurately known from high-resolution spectroscopic studies up to its dissociation limit [4,5], providing a well depth D_e =3993.47(18) cm^{-1} [5]. The measured spectroscopic constants for the 1 $^1\Pi_u$ state were also reported in Ref. [4], while the characterization of this state up to the quasibound energy levels induced by its potential barrier (Fig. 1) was done by applying a full quantum approach to obtain the potential energy curve and accurate effective molecular constants [6]. The barrier height was found to be ≈205 cm^{-1} above its asymptotic limit ($5S_{1/2}+5P_{3/2}$) at 9.14 Å. In contrast, only partial information is available for the 1 $^1\Sigma_u^+$ state. The first qualitative attempt to characterize the 1 $^1\Sigma_u^+$ state was provided by Drummond and Schlie [7] through quasistatic temperature dependence study of the absorption profile of the 1 $^1\Sigma_g^+ \to 1$ $^1\Sigma_u^+$ transition. From their approximate potential curves the value $T_e \approx 10\,800$ cm^{-1} could be deduced, while on the basis of the preliminary results Amiot [4] gave an upper limit $T_e < 10\,790$ cm^{-1}. Strong perturbation effects in the infrared fluorescence spectra recorded after the resonant excitation process 1 $^1\Sigma_g^+ \to 1$ $^1\Sigma_u^+ \to 2$ $^1\Pi_g$ were observed [8] and assigned to the spin-orbit coupling between 1 $^1\Sigma_u^+$ (or A $^1\Sigma_u^+$) and 1 $^3\Pi_u$ (or b $^3\Pi_u$) electronic states, well-known as the A-b singlet-triplet mixed system. The spin-orbit interaction strongly increases from lithium to cesium. In contrast to the lightest Li$_2$ dimer, where only a few isolated levels in the A state are perturbed by those of the b state, the interaction is so strong in Rb$_2$ that the entire regularity of the A-b energy level spectrum is apparently lost. Several theoretical studies [8–10] confirmed that the Rb$_2$ 1 $^1\Sigma_u^+$ and 1 $^3\Pi_u$ spectra present a case of fully coupled electronic states, preventing the usual local inversion procedures based on the semiclas-

*Author to whom correspondence should be addressed. Email address: blecic@ifs.hr
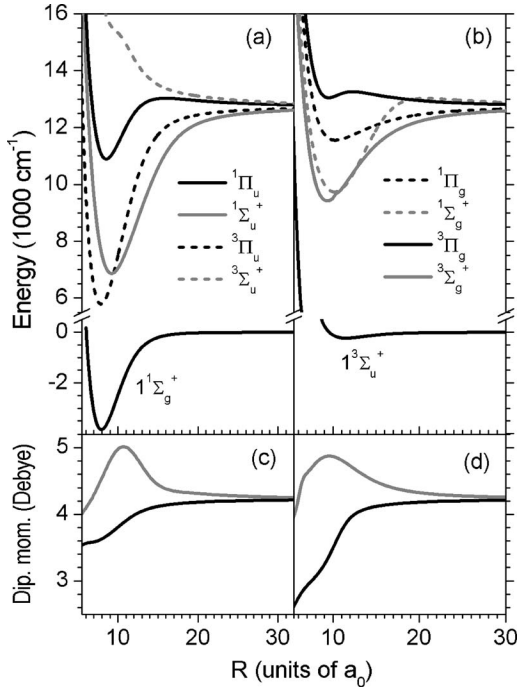
FIG. 1. Hund's case-(a) potentials and transition dipole moments relevant to the transitions between the Rb(5S)+Rb(5S) and Rb(5S)+Rb(5P) manifolds. (a) Lower $1\,^1\Sigma_g^+$ and upper *ungerade* potentials. (b) Lower $1\,^3\Sigma_u^+$ and upper *gerade* potentials. (c) $1\,^1\Sigma_g^+ - 1\,^1\Sigma_u^+$ (gray) and $1\,^1\Sigma_g^+ - 1\,^1\Pi_u$ (black) transition dipole moments. (d) $1\,^3\Sigma_u^+ - 1\,^3\Sigma_g^+$ (gray) and $1\,^3\Sigma_u^+ - 1\,^3\Pi_g$ (black) transition dipole moments. At the scale of the figure, experimental and theoretical potentials are almost identical.

sical Rydberg-Klein-Rees method [11], which is intrinsically limited to the single-state single-well potential determination.

Finally, very little is known experimentally about triplet states relevant for present work. To our knowledge, there is only one rough estimate of the well depth D_0 $=350 \pm 100$ cm^{-1} [12], of the $1\,^3\Sigma_u^+(5s+5s)$ electronic state, while Ref. [13] gives a constraint on the position of its repulsive wall after analyzing two-photon ionization spectrum of ultracold Rb$_2$ molecules. In addition, direct observation of the $2\,^3\Pi_u(5s+4d)$ state in a pulsed molecular beam was reported in Ref. [14], and Lozeille *et al.* [13] observed low vibrational levels of the $2\,^3\Pi_g(5s+4d)$ and $2\,^3\Sigma_g^+(5s+4d)$ states.

All theoretical studies [8–10] mentioned previously were based on computed potential curves based on an effective large core potential approach (i.e., treating the atom as a one electron system) including core polarization effects [15]. These calculated potentials have been rated as high quality state-of-the-art quantum chemistry calculations. Recently, two new theoretical studies of the electronic states of the Rb$_2$ molecule have appeared. Park *et al.* [16] have calculated the potential energy curves for a large number of states up to the $5s+7s$ dissociation limit, within a multireference configuration interaction framework using an averaged relativistic effective small-core potential and an effective core-polarization potential. Edvardsson *et al.* [17] have obtained

potential curves for the ground $1\,^1\Sigma_g^+$ state and nine excited ungerade states using an all-electron (*ab initio*) relativistic method. They have also derived the corresponding spin-orbit coupling matrix elements for the $5s+5p$ manifold using a first-order perturbation theory. The perturbation theory was expected to be a good approximation but it turned out that the method used underestimates the asymptotic fine structure splitting by 30%. The authors themselves consider their work as a preliminary study for a detailed experimental and theoretical investigation of the real-time dynamics of the (A-b) coupled states in Rb$_2$ performed later on by Gador *et al.* [18]. The calculations of Ref. [18] are found quite sensitive to the choice of potential curves [16,17], and while all characteristic features of the experimental traces are well reproduced, the relative intensities of the spectral peaks differ significantly among all cases.

Actually, none of the abovementioned theoretical works was accompanied with the corresponding calculations of the transition dipole moments. Here we extended the Rb$_2$ calculations of Ref. [15] in order to derive the transition dipole moments needed for the present spectral simulations, following the same lines as in Refs. [19,20]. We demonstrate that the present low resolution absorption spectroscopy is very sensitive to the electronic structure and dynamics of the molecule, and that it is a powerful tool for evaluating the accuracy of the computed molecular quantities.

II. SPECTRAL SIMULATIONS

We use two standard approaches which are known to be in good agreement with each other [21]. (i) A semiclassical model which is useful to obtain the global envelope of the absorption spectra, and to ensure the consistency between the measured temperature of the gas and the fitted one, providing that the transition dipole moment functions are properly described. (ii) A quantum simulation involving a coupled state picture, whose results are governed by the dynamics of the molecule, such as the interferences between several Condon point contributions, of the magnitude of the spin-orbit coupling.

In the simple quasistatic approximation, the classical absorption spectra generally agree with the overall quantum mechanical band shapes, except for nearly periodic band structures and non-classical behavior at the satellite positions. The refined treatment of the spectra, based on uniform Airy approximation, avoids singularities pertinent to the quasistatic line shapes and takes into account interferences among contributions of various Condon points.

A. Semiclassical approach

The absorption coefficient is first calculated applying the semiclassical approach described in Ref. [22]. The quasistatic formula for the absorption coefficient (expressed in cgs units) reads [3,22,23]

$$k_T(\omega) = N^2 \frac{4\pi^3 e^2 \hbar}{m_e c} \sum_{\alpha,\beta} \sum_C \frac{R_C^2 f_{\alpha\beta}(R_C)}{|\Delta' V_{\alpha\beta}(R_C)|}$$

$$\times \exp\{-[V_\alpha(R_C) - V_\alpha(\infty)]/k_B T\}. \qquad (1)$$

In the above expression N is the atom number density, T is

the temperature, and the indices α and β count all substates of the initial and final states, respectively, involved in optical transitions that contribute to the absorption spectra in the considered spectral range. The $\Delta V_{\alpha\beta} = V_\alpha - V_\beta$ and $\Delta' V_{\alpha\beta}$ label the difference potential and its first derivative, respectively. The molecular oscillator strength $f_{\alpha\beta}$ is proportional to the square of the corresponding electronic transition moment and the sum of all oscillator strengths taken at any fixed internuclear separation R in asymptotic region is always twice the total atomic oscillator strength [23]. In the second sum the index C goes over all Condon points R_C which fulfill the classical Franck-Condon condition $\Delta V_{\alpha\beta} = hc/\lambda$ at the particular transition. The remaining symbols in Eq. (1) have their usual meaning. The relation (1) can be applied for the evaluation of the absorption coefficient only in the region of energies where the difference potential curve exhibits no extrema. When an extremum is approached, the above relation yields a nonphysical singularity owing to the fact that two Condon points come close to each other and the derivatives of the difference potential tend to zero. To calculate the contribution to the spectrum arising from the coalescent pair of Condon points the method of uniform mapping [22] was applied. It correctly takes into account the interference among Condon points thus avoiding the singularity.

As an input for the semiclassical spectral simulation one needs the potential function for the initial state, entering the Boltzmann factor which influences the temperature dependence of the calculated spectra, the difference potential determining the Condon points, and the molecular oscillator strengths, modulating the contributions to the spectra from various Condon points. We take into account all the possible transitions between the $5\,^2S + 5\,^2S$ and $5\,^2S + 5\,^2P$ manifolds, namely, all singlet $(1\,^1\Sigma_g^+ \rightarrow 1\,^1\Sigma_u^+, 1\,^1\Sigma_g^+ \rightarrow 1\,^1\Pi_u)$ and triplet $(1\,^3\Sigma_u^+ \rightarrow 1\,^3\Sigma_g^+, 1\,^3\Sigma_u^+ \rightarrow 1\,^3\Pi_g)$ bands. The effects of spin-orbit mixing are properly accounted for in the subsequent calculations (see Sec. IV below).

B. Vibrational band continuum approximation

In the quantum-mechanical formulation the bound-bound absorption coefficient at angular frequency ω for transitions from a set of rovibrational levels $(v''J''\Lambda'')$ of the lower electronic state thermally populated at temperature T towards a set of rovibrational levels of the upper electronic state $(v'J'\Lambda')$ is [2,21]

$$k_T^{bb}(\omega) = N^2 C_T(\omega) \sum_{v''J''} \sum_{v'J'} \omega_{J''} S_{J''\Lambda''}^{J'\Lambda'} \exp(-E_{v''J''\Lambda''}/k_B T)$$
$$\times |\langle v''J''\Lambda''|D(R)|v'J'\Lambda'\rangle|^2 g(\omega - \bar{\omega}), \quad (2)$$

where $\omega_{J''}$ is the nuclear spin statistical factor, $S_{J''\Lambda''}^{J'\Lambda'}$ is the Hönl-London factor, $g(\omega - \bar{\omega})$ is the normalized line-shape function, $\hbar\bar{\omega} = E_{v'J'\Lambda'} - E_{v''J''\Lambda''}$ is the transition energy, and

$$C_T(\omega) = \frac{(2 - \delta_{0,\Lambda'+\Lambda''})}{(2 - \delta_{0,\Lambda''})} \frac{(2S_m + 1)}{(2S_a + 1)} \frac{4\pi^2\omega}{3\hbar c} \left[\frac{h^2}{2\pi\mu k_B T}\right]^{3/2}.$$
$$(3)$$

S_m and S_a are spin multiplicities for molecule and atom, respectively, and μ is the reduced mass.

If the line-shape function $g(\omega - \bar{\omega})$ is replaced by $1/\Delta\omega$, the absorption coefficient is effectively averaged over the interval $\Delta\omega$ and summation in Eq. (2) runs over all transitions that fall within the interval $\omega \pm \Delta\omega/2$. If furthermore the interval $\Delta\omega$ is smaller than the typical spacing of the vibrational bands, but larger than the typical spacing of the rotational lines, the rovibrational lines are smoothed out and the difference in nuclear spin factor for even and odd J's can be neglected by putting $\omega_{J''} = \frac{1}{2}$; the rotational P and R branches could also be replaced with two Q branches, $J' = J'' = J$. Assuming then that the transition energy can be written as $\hbar\omega = \hbar\omega_{v'v''} + hc\Delta B J(J+1) + \cdots$, where $\omega_{v'v''}$ is the transition frequency for $J = 0$, and $\Delta B = B_{v'} - B_{v''}$ is the difference of the molecular rotational constants, the summations over the discrete indices J' and J'' can be transformed to a continuous distribution of frequency ω [21]:

$$k_T^{bb}(\omega) = N^2 C_T(\omega) \times \sum_{v',v''} \frac{\omega_{v'v''}}{4\pi c \Delta B} \exp(-E_{v''0\Lambda''}/k_B T)$$
$$\times |\langle v''0\Lambda''|D(R)|v'0\Lambda'\rangle|^2$$
$$\times \left[\frac{\omega}{\omega_{v'v''}} \exp\left(-\frac{B_{v''}(\omega_{v'v''} - \omega)}{2\pi\Delta B k_B T}\right)\right]. \quad (4)$$

We have used Eq. (4) as a starting point for simulation of the bound-bound contribution to the absorption coefficient. Care was taken of the correction due to second order term, which describes the centrifugal distortion and is important at large v' and v'' where ΔB becomes small, as described in more detail in Ref. [21].

We focused here on the singlet bands, namely, the $(X\text{-}A)$ and $(X\text{-}B)$ bands, which will reveal their dependence with the molecular structure parameters like transition dipole moments and spin-orbit couplings. Energies and wave functions for vibrational levels were determined in the framework of the Fourier grid Hamiltonian (FGH) method [9,10,24].

C. Potential curves and transition dipole moments

To obtain the $1\,^1\Sigma_g^+$ potential curve we used the analytical expression [5] derived from the spectroscopic data and valid for the whole range of interatomic distances. The potential curve for the $1\,^1\Pi_u$ state in the range between $6.8a_0$ and $30a_0$ $(a_0 = 0.0529177$ nm$)$ was obtained by cubic spline interpolation through the experimental data of Ref. [6]. The points in the inner portion of the $1\,^1\Pi_u$ potential well $(R < 6.8a_0)$ were generated by a fit to an exponential of the form $Ae^{-BR} + C$, where A, B, and C are parameters, and R is the internuclear distance. The values of the parameters used were $A = 49315.8$ cm^{-1}, $B = 0.1439a_0^{-1}$, $C = -6159.1$ cm^{-1}. The $1\,^1\Pi_u$ potential curve has been smoothly matched at $R = 30a_0$ to the long-range behavior described in Ref. [25]. For all other states involved in the calculation we have used our own theoretical data.

We performed potential curves and transition dipole moment calculations using the CIPSI package (configuration interaction by perturbation of a multiconfiguration wave function selected iteratively) [26] developed by the Laboratoire

de Physique Quantique (Toulouse, France). The atomic cores are described by the large-core pseudopotential of Durand and Barthelat [27] whose parameters have been adjusted to reproduce the energies and valence orbitals of all-electron Hartree-Fock self-consistent calculation for the atomic ground state. For Rb the pseudopotential includes the mass-velocity, and the Darwin relativistic corrections. Core polarization is taken into account through an *l*-dependent effective core polarization potential [28] depending on the dipole polarizability of the Rb$^+$ ion and on *l*-dependent cutoff parameters adjusted to reproduce the experimental energies of the lowest 5*s*, 5*p*, and 4*d* atomic levels. Each atom is described by a Gaussian basis set of *A* type (see Ref. [19]), and full valence configuration interaction calculations are finally performed. The reported data include the purely repulsive 1/*R* term core-core interaction term, and no other additional empirical terms for core-core interaction. Note, however, that core-core interaction influences neither the electronic wave function, nor the dipole moment functions. The potential curves calculated with basis *A* have already been used by Lozeille *et al.* [13] and are available there up to the 5*s*+4*d* asymptote as supplementary material. For completeness, the transition dipole moments (Fig. 1) are provided as supplementary material to the present paper [29].

In the next section however, the rovibrational wave functions are evaluated by simulating the part of the core-core interaction which is missing in the quantum chemistry calculations in the following way: the difference between the experimental ground state and the calculated one is added to all relevant excited states, assuming that the core-core interaction is in first approximation independent of the excitation of the molecule. Such an approach has been successfully applied for the description of the NaRb Fourier transform spectroscopy [30]. Then obviously, the difference potentials are not affected by this transformation.

III. EXPERIMENTAL PROCEDURE AND QUANTITATIVE ANALYSIS

The specific details of our experimental arrangement (see inset of Fig. 2) are given in Ref. [3] and are shortly repeated here. The rubidium vapor column (length: 6.5±0.5 cm) was produced in a stainless-steel heat pipe (inner diameter: 2 cm, length: 18 cm). Argon was used as a buffer gas to protect the quartz windows from the corrosive influence of hot metal vapor. The rubidium vapor was generated by an outer heater and the heat pipe was operating in the heat pipe mode, i.e., the rubidium pressure was nearly equal to the buffer gas pressure (typical pressure: 10 mbar). In addition, the metal vapor was overheated by the help of an inner heater (diameter: 2 mm, length: 15 cm). In this manner, the temperature and consequently, the vapor number density distributions, were axially symmetric. The temperature was ranging from T_{IH} at the edge of the inner heater to the metal bath temperature T_w at the heat pipe wall. The boundary temperatures depend on the chosen inner and outer heating powers applied and their typical values in present experiment were about 1000 and 600 K, respectively. Such a strongly overheated and radially inhomogeneous vapor column was investigated
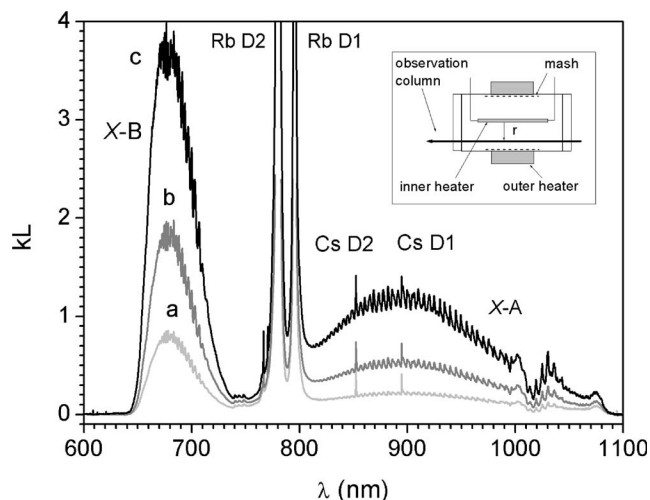
FIG. 2. Measured optical depths kL in overheated rubidium vapor at positions (a) *r*=3 mm, (b) *r*=6 mm, and (c) *r*=9 mm from the heat pipe axis. The corresponding atom number densities and temperatures are $N(r_a)=4.25 \times 10^{16}$ cm^{-3}, $N(r_b)=4.66 \times 10^{16}$ cm^{-3}, $N(r_c)=5.05 \times 10^{16}$ cm^{-3}, and $T(r_a)=745$ K, $T(r_b)=675$ K, $T(r_c)=625$ K, respectively. The buffer gas pressure was 5 mbar, and the applied outer and inner heating powers were 150 and 6 W, respectively. Inset: Experimental arrangement for spatially resolved absorption measurements.

applying the spatially resolved white-light absorption method [3]. The absorption spectra were related to thin columns (diameter $\Delta r \approx 0.5$ mm) at the distance *r* from the heat pipe axis.

Typical spatially resolved (i.e., temperature dependent) obtained spectra are shown in Fig. 2. The main features are the *X-B* band (between 640 and 740 nm), well separated from the *X-A* band located between 800 and 1080 nm. The wings of the resonance lines are rather insensitive to the temperature variation, because they are due to the transition in the long-range region where interaction potentials are weak and the corresponding Boltzmann factor is practically equal to unity for the range of temperatures used in the experiment. The extended red wing of the resonance doublet overlaps the *X-A* molecular band. The shapes of both *X-A* and *X-B* molecular bands are strongly temperature dependent. The temperature dependences of these bands are different because the maxima of the bands originate from different internuclear distances and consequently the *X-A* and *X-B* transitions are characterized by different Boltzmann factors. As demonstrated in the next section, the dip around 1020 nm is a signature of the strong perturbation caused by the *A-b* singlet-triplet mixing.

The quantitative analysis, i.e., the determination of the number densities and temperatures is based on the accurate data for the absorption coefficient of the quasistatic rubidium resonance line wings. According to Ref. [31], the absorption coefficient k_{D1} (in cm^{-1}) at a detuning $\Delta\lambda$ (in nm) in the red wing of the rubidium *D*1 line and for an atom number density *N* (in cm^{-3}) can be expressed as

$$k_{D1}^{\text{red}} = 5.02 \times 10^{-34} P(\Delta\lambda/\Delta_{\text{FS}}) \frac{N^2}{(\Delta\lambda)^2}, \qquad (5)$$

where the polynomial $P(\Delta\lambda/\Delta_{\text{FS}})$ is resulting from the fit of the theoretical profile and is given by

$$P(\Delta\lambda/\Delta_{\text{FS}}) = 1.0317 + 2.2934\left(\frac{\Delta\lambda}{\Delta_{\text{FS}}}\right) - 0.6319\left(\frac{\Delta\lambda}{\Delta_{\text{FS}}}\right)^2$$

$$+ 0.0732\left(\frac{\Delta\lambda}{\Delta_{\text{FS}}}\right)^3. \qquad (6)$$

Here, Δ_{FS} is the fine structure splitting of the $5P$ rubidium state (in nm). It should be pointed out that Eq. (6) is found to be valid for detunings 1 nm $\leq \Delta\lambda \leq 3\Delta_{\text{FS}}$. As one can see in Fig. 2, at present conditions the resonance lines are superimposed to the molecular signal, which should be subtracted from the measured total optical depth $k(\lambda)L$. The X-A molecular signal in the vicinity of Rb $D1$ line is approximated by straight lines (dashed lines in Fig. 2) with height and slope fitted to the values for which the remaining $k(\lambda)L$ acquired the wavelength dependence defined by Eqs. (5) and (6). In this manner, with estimated vapor column length, values for rubidium number densities $N(r)$ at given distance r from the heat pipe axis were obtained with an accuracy of about 3%. The measurements were performed up to $r = 9$ mm, and the number density N ($r_w = 10$ mm) just above the liquid metal at the heat pipe wall was obtained by extrapolation. With known $N(r_w)$, the temperature T_w of the liquid metal bath being in thermal equilibrium with vapor just above its surface can be determined by use of atomic vapor pressure curve [32]. At present experimental conditions the density of rubidium molecules is negligible (less than 1% of the atomic number density). Then, the temperature $T(r)$ at position r can be calculated by use of ideal gas law which yields $T(r) = T(r_w)N(r_w)/N(r)$. For example, in the spectra presented in Fig. 2, the described evaluation procedure yields $N(r_a) = 4.25 \times 10^{16}$ cm^{-3}, $N(r_b) = 4.66 \times 10^{16}$ cm^{-3}, and $N(r_c) = 5.05 \times 10^{16}$ cm^{-3}. The corresponding temperatures are $T(r_a) = 745$ K, $T(r_b) = 675$ K, and $T(r_c) = 625$ K, whereas the error bars amount to ± 35 K.

IV. SIMULATIONS AND DISCUSSION

In order to take into account the effects of the spin-orbit interaction responsible for the mixing of the Hund's case (a) states we have built a new set of Hund's case (c) potential curves, labeled according to the standard notation $\Omega_{g/u}^{+/-}$ related to the projection Ω of the total electronic angular momentum on the molecular axis. They are obtained after the diagonalization of the following matrices, which have been evaluated in Ref. [33], and are given here for the readers' convenience:

$$H(\Omega = 1_{g/u}) = \begin{pmatrix} V(^3\Sigma_{g/u}^+) & \dfrac{\Delta E_{\text{FS}}}{3} & \dfrac{\Delta E_{\text{FS}}}{3} \\[2mm] \dfrac{\Delta E_{\text{FS}}}{3} & V(^3\Pi_{g/u}) & -\dfrac{\Delta E_{\text{FS}}}{3} \\[2mm] \dfrac{\Delta E_{\text{FS}}}{3} & -\dfrac{\Delta E_{\text{FS}}}{3} & V(^1\Pi_{g/u}) \end{pmatrix}, \quad (7)$$
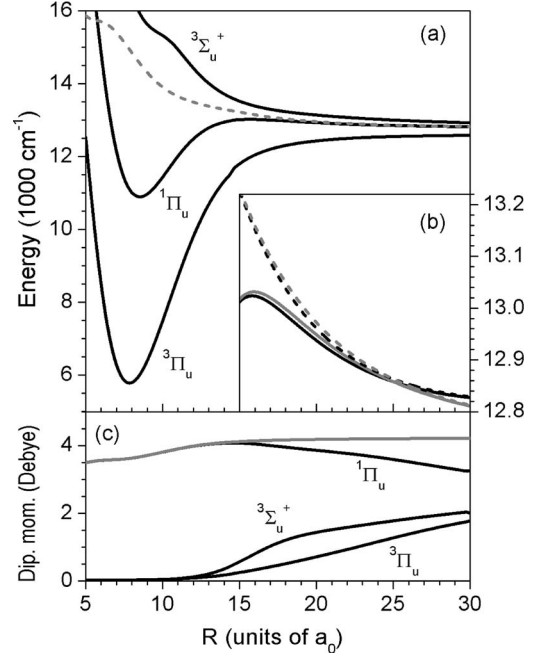
FIG. 3. (a) Hund's case-(c) potential curves for the 1_u symmetry (full black lines), correlated to the $5s + 5p$ dissociation limit. They are labeled according to their Hund's case-(a) symmetry $1\,^1\Pi_u$, $2\,^3\Sigma_u^+$, and $1\,^3\Pi_u$, at short distances. The difference potential for the $1\,^1\Sigma_g^+ \rightarrow 1_u(1\,^1\Pi_u)$ transition is drawn with a dashed line. (b) Blow up of the Hund's case-(a) $1\,^1\Pi_u$ potential (full gray line) and its Hund's case-(c) counterpart $1_u(1\,^1\Pi_u)$ (full black line), and the corresponding difference potentials (gray and black dashed lines, respectively) for transitions from the $1\,^1\Sigma_g^+$ state. (c) Dipole moments for the transitions $1\,^1\Sigma_g^+ \rightarrow 1\,^1\Pi_u$ (gray line) and $1\,^1\Sigma_g^+ \rightarrow 1_u(1\,^1\Pi_u)$, $1\,^1\Sigma_g^+ \rightarrow 1_u(2\,^3\Sigma_u^+)$, $1\,^1\Sigma_g^+ \rightarrow 1_u(1\,^3\Pi_u)$ (black lines). The Hund's case-(c) data are computed with a constant spin-orbit coupling (see text).

$$H(\Omega = 0_{g/u}^+) = \begin{pmatrix} V(^1\Sigma_{g/u}^+) & \dfrac{\sqrt{2}}{3}\Delta E_{\text{FS}} \\[2mm] \dfrac{\sqrt{2}}{3}\Delta E_{\text{FS}} & V(^3\Pi_{g/u}) - \dfrac{\Delta E_{\text{FS}}}{3} \end{pmatrix}, \quad (8)$$

$$H(\Omega = 0_{g/u}^-) = \begin{pmatrix} V(^3\Sigma_{g/u}^+) & \dfrac{\sqrt{2}}{3}\Delta E_{\text{FS}} \\[2mm] \dfrac{\sqrt{2}}{3}\Delta E_{\text{FS}} & V(^3\Pi_{g/u}) - \dfrac{\Delta E_{\text{FS}}}{3} \end{pmatrix}. \quad (9)$$

In these expressions we assumed that the spin-orbit coupling is R independent and proportional to the atomic fine structure splitting ΔE_{FS}. We have also correspondingly transformed the relevant transition dipole moments. We displayed in Figs. 3 and 4 the obtained results for the 1_u and 0_u^+ symmetries relevant for the X-B and X-$(A$-$b)$ transitions. Let us mention that because the avoided crossing between the A and b states is sensitive to the coupling, we have also used an R-dependent spin-orbit coupling (see Sec. IV C below).
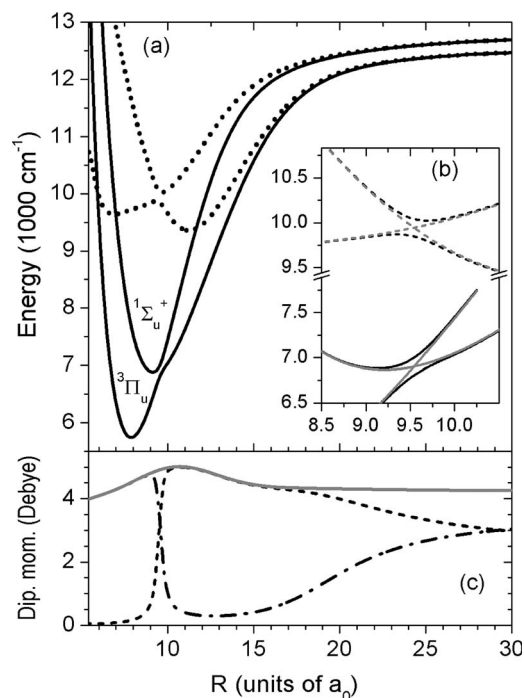
FIG. 4. (a) Hund's case-(c) potential curves for the 0_u^+ symmetry (full black lines), correlated to the $5s+5p$ dissociation limit. They are labeled according to their Hund's case-(a) symmetry $1\,^1\Sigma_u^+$ and $1\,^3\Pi_u$, at short distances. The difference potentials for the corresponding $1\,^1\Sigma_g^+\rightarrow 0_u^+$ transitions are drawn with dotted lines. (b) Blow up of the crossing region, where we see that Hund's case-(a) (gray) and -(c) (black) curves are superimposed except in the vicinity of the crossing. (c) Transition dipole moments for the transitions $1\,^1\Sigma_g^+\rightarrow 1\,^1\Sigma_u^+$ (gray line), $1\,^1\Sigma_g^+\rightarrow 0_u^+$ (upper) (dash-dot line) and $1\,^1\Sigma_g^+\rightarrow 0_u^+$ (lower) (dashed line).

A. Semiclassical simulation of the reduced absorption coefficient

The $B\,^1\Pi_u$ potential and its Hund's case (c) 1_u counterpart differ only slightly for $R>13a_0$ [Fig. 3(b)] but there is a significant difference in the behavior of the corresponding transition dipole moments [Fig. 3(c)]. However, as the bound vibrational states in the $B\,^1\Pi_u$ potentials are confined at shorter internuclear distances, the simulations using either the Hund's case-(a) or Hund's case-(c) potentials yield essentially the same spectrum.

The $1\,^1\Sigma_u^+$ and $1\,^3\Pi_u$ electronic states cross each other near $R=9.6a_0$ resulting with an avoided crossing in the 0_u^+ curves [Fig. 4(a)] producing the extrema in the corresponding differential potential [Fig. 4(b)]. The spin-orbit mixing results in the drastic change in the transition dipole moments. The dipole moment for the $1\,^1\Sigma_g^+\rightarrow 1\,^1\Sigma_u^+$ transition only slightly deviates from its asymptotic value, while the $1\,^1\Sigma_g^+\rightarrow 1\,^3\Pi_u$ transition is spin-forbidden. In the Hund's case (c) picture the transition dipole moment from the X state towards the upper 0_u^+ state (with $1\,^1\Sigma_u^+$ character at short distance) suddenly drops down beyond the crossing point, while the transition towards the lower 0_u^+ state (with $1\,^3\Pi_u$ character at short distances) "borrows" the intensity.

The measured reduced absorption coefficient $k_T(\lambda)/N^2$ for four different temperatures (T^{expt}=615, 660, 700, 745 K, de-
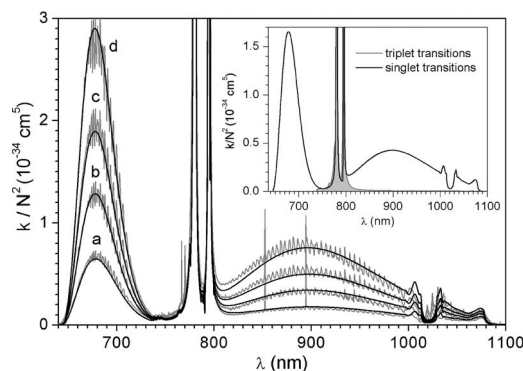
FIG. 5. Comparison of experimental (gray lines) and semiclassically simulated (black lines) reduced absorption coefficient for four different temperatures. (a) T_a^{expt}=615 K, T_a^{fit}=620 K, (b) T_b^{expt}=660 K, T_b^{fit}=650 K, (c) T_c^{expt}=700 K, T_c^{fit}=680 K, (d) T_d^{expt}=745 K, T_d^{fit}=740 K. Experimental temperatures are determined with a typical ±35 K uncertainty. Inset shows typical contributions of singlet (black line) and triplet (gray shaded area) transitions, respectively.

termined with a typical ±35 K uncertainty) and the corresponding semiclassical simulations based on the Hund's case (c) potentials and transition dipole moments are displayed in Fig. 5. The temperatures taken for the calculations (T^{fit}=620, 650, 680, 740 K) are those for which the simulations yield the best fit for both molecular bands, and indeed yield an overall satisfactory agreement between experiment and theory for both the envelope of the spectra and for the temperature values. The inset of Fig. 5 shows that the contribution of the triplet bands (starting from the $1\,^3\Sigma_u^+$ state) is mainly located under the broad atomic lines, while the X-B band is indeed well isolated from the other ones. Since the simulation of the X-B reduced absorption coefficient relies on experimental potential energy curves, the results then confirm the accuracy of the applied semiclassical approach, as well as of the molecular structure data, i.e., the present computed R-dependent transition dipole moments. As a further demonstration, we reported in Fig. 6 the result of the simulation of the experimental spectrum at T^{expt}=615 K, using constant transition dipole moments equal to their
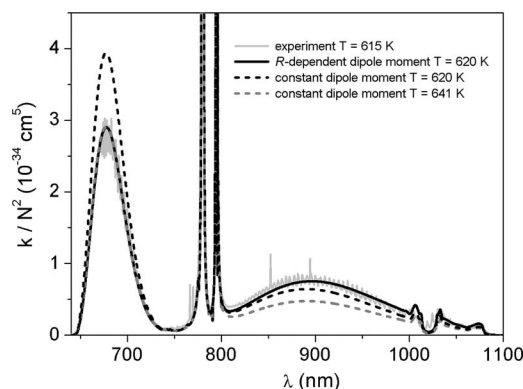
FIG. 6. Experimental and simulated curves in case (a) from Fig. 5, compared to two further simulations: constant dipole moments at T^{fit}=620 K (dashed line) and at T^{fit}=641 K (gray line).
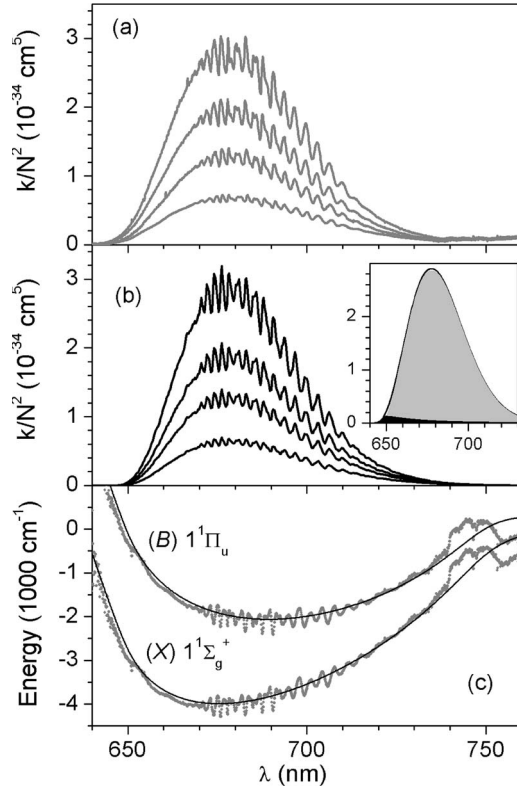
FIG. 7. (a) Experimentally observed Rb_2 X-B band for four different temperatures given in Fig. 5. (b) Corresponding theoretical simulations. Inset: Typical contributions of bound-bound (gray area) and bound-free (black area) transitions. (c) Comparison of the potentials deduced from the Boltzmann plot (gray dots) and empirically [5,6] determined potentials (black curves).

FIG. 8. The reduced absorption coefficient of the Rb_2 X-A and X-$(A$-$b)$ bands. All theoretical simulations were done with T^{fit} =620 K, while the corresponding experimental spectrum (e) was measured at T^{expt}=615 K. Theoretical simulations with R-dependent spin-orbit coupling: (a) Hund's case (a) $(1\,^1\Sigma_g^+ \rightarrow 1\,^1\Sigma_u^+)$, (b) Hund's case (c) with separate contributions from transition to lower (dark gray) and upper (black) 0_u^+ state, (c) Hund's case (c) with the former two contributions superimposed, (d) coupled A-b system, (f) Theoretical simulation for coupled A-b system with R-independent spin-orbit coupling.

asymptotic values for both singlet bands. As can be seen, neither X-B band nor X-A band can be satisfactorily reproduced with T^{fit}=620 K. The best fit of the X-B band is now obtained for T^{fit}=641 K, and we were not able to simultaneously fit the X-A band. In other words with constant dipole moment there is no single temperature with which agreement with the measured spectrum can be obtained in the whole investigated region. This comes from the pronounced variation [Figs. 1(a) and 1(c)] of the dipole moment at short internuclear distances, where from a significant contribution to the absorption coefficient [3] arises. The same argument was recently successfully applied for simultaneous determination of the temperature and the number density of Rb vapors [34].

B. Quantum simulation of the X-B band

Energies and wave functions $\Psi_{v''}^X(R)$ and $\Psi_{v'}^B(R)$ for the $X\,^1\Sigma_g^+$ and $B\,^1\Pi_u$ vibrational levels are determined on a uniform grid of constant step with $N=1208$ points, ranging from $4.5a_0$ to $40a_0$. According to the FGH method, the wave functions are normalized as $\Sigma_{i=1}^N \Psi_{v''}^X(R_i)\Psi_{v'}^X(R_i)=1$ and the matrix elements of the dipole moment $D^{X\text{-}B}(R)$ are computed as $\langle X,v''|D^{X\text{-}B}|B,v'\rangle = \Sigma_{i=1}^N \Psi_{v''}^X(R_i)D^{X\text{-}B}(R_i)\Psi_{v'}^X(R_i)$. The bound-bound contribution to the reduced absorption coefficient is calculated within the vibrational band continuum approxima-

tion given by Eq. (4), with the rotational constants $B_{v''}^X$ =$\Sigma_{i=1}^N |\Psi_{v''}^X(R_i)|^2/(2\mu R_i^2)$ (and as well for $B_{v'}^B$) taken from experiment when available [5,6].

Figure 7 shows the excellent agreement of the experimentally observed X-B band with the simulated one for the four temperatures given in Fig. 5, demonstrating the applicability of the vibrational band continuum approximation in the present case. The inset in Fig. 7(b) confirms that the small contribution of the bound-free transitions can safely be neglected.

As a consistency check of our temperature determination, we have performed the Boltzmann-plot analysis in order to deduce the interaction potentials. First, we have used temperatures obtained from the experiment and we have determined the λ dependence of the ground state potential [gray points in Fig. 7(c)]. Then, we have added the photon transition energy and we have obtained the λ dependence of the $B\,^1\Pi_u$ potential. Finally, we have used the empirically determined potentials [5,6] and we have formed the difference potential (which is a monotonic function of the internuclear distance R) in order to map the R dependence of both potentials into the λ dependence [black lines in Fig. 7(c)]. The agreement between the displayed results additionally confirms the reliability of the method employed for the temperature determination.
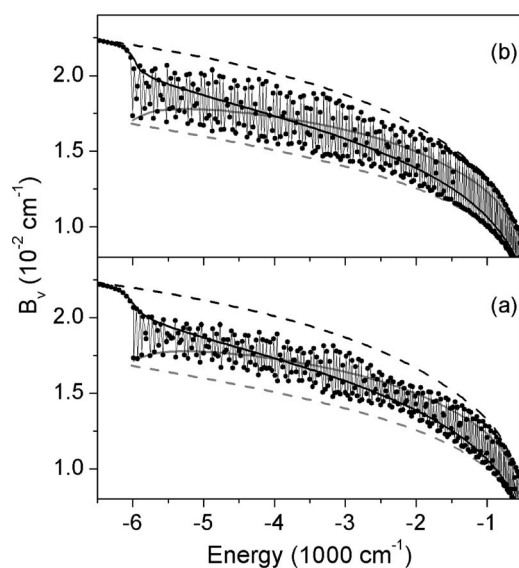
FIG. 9. (a) Rotational constants B_v as functions of the binding energy of $^{85}Rb_2$ vibrational levels computed with R-independent spin-orbit coupling: Hund's case (a) (B_v^b, black dash; B_v^A, gray dash), Hund's case (c) (B_v^{lower}, full black line; B_v^{upper}, full gray line), and the coupled A-b system (black dots). (b) Same as (a) but with variable spin-orbit coupling.

C. Quantum simulation of the *X-A* band and analysis of the perturbed *A-b* system

In order to get deeper insight into absorption spectrum within the range of the experimentally observed *X-A* band we have performed three different quantum mechanical simulations: (i) in the Hund's case (a) framework, (ii) in the Hund's case (c) basis after the diagonalization of the matrix in Eq. (8), and (iii) in a coupled state picture, following previous works [8–10]. The vibrational wave functions were represented on the same grid as described in the previous section. In spectral simulations corresponding to (ii) and (iii) cases the *R*-dependent spin-orbit coupling scaled from the calculated K_2 coupling [15] was used, and the calculations in all three cases were performed for $^{85}Rb_2$ isotopomer.

In case (i) for the upper state we have used the single $1\,^1\Sigma_u^+$ potential curve and corresponding dipole moment (Fig. 4). The result is shown in Fig. 8(a). As the spin-orbit interaction is entirely neglected, the dip in the absorption spectrum around 1020 nm is completely absent. On the other hand, the positions of the vibrational bands are reproduced quite well, but the amplitude of their modulation is much smaller than experimentally observed [Fig. 8(e)].

In case (ii) we have calculated independently contributions to the spectrum arising from the lower and upper 0_u^+ states using the corresponding dipole moments (Fig. 4). The obtained results are shown in Fig. 8(b). The superposition of these two contributions is depicted in Fig. 8(c) and we can see that the prominent features beyond the dip at 1020 nm originate from the lower 0_u^+ state. But the amplitude of the modulations in the 850–1000 nm range is too large compared to the experimental one.

Finally, we have treated the *A-b* system with a coupled channel picture [case (iii)]. A $2N \times 2N$ Hamiltonian matrix is
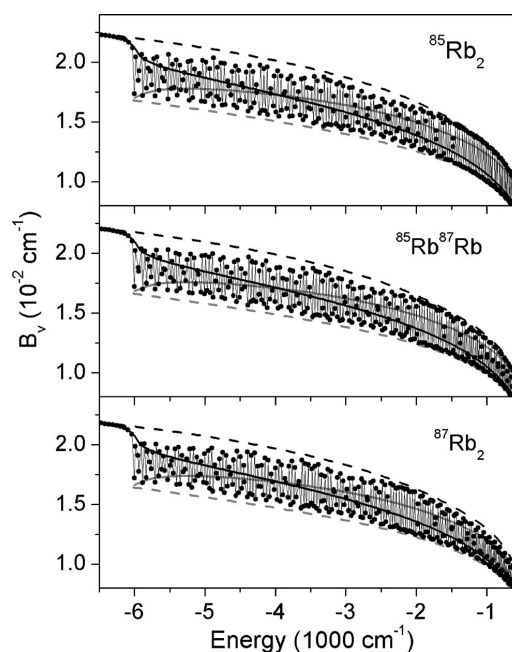
FIG. 10. Rotational constants B_v as functions of the binding energy for different isotopomers computed with R-dependent spin-orbit coupling: Hund's case (a) (B_v^b, black dash; B_v^A, gray dash), Hund's case (c) (B_v^{lower}, full black line; B_v^{upper}, full gray line), and the coupled *A-b* system (black dots).

built with the grid representation of the *A* and *b* states, and of their spin-orbit coupling, yielding after diagonalization the whole spectrum of coupled vibrational levels. The calculated spectrum is shown in Fig. 8(d). For completeness, the result obtained by using the constant spin-orbit coupling is also shown [Fig. 8(f)]. As can be seen from Fig. 8 only within the coupled *A-b* channel approach the experimental spectrum could be reproduced satisfactorily regarding both the modulation and the structure around the dip at ~1020 nm. Moreover, the amplitude of the oscillations and the structure around the dip are the most closely reproduced with variable spin-orbit coupling. The slight shift of the dip position is probably due to the approximate potential curves and spin-orbit coupling. The constant coupling yields the modulation and the intensity of the peaks around ~1020 nm, which are slightly more pronounced than experimentally observed. However, the measured spectrum comprises the contributions of all isotopomers ($^{85}Rb_2$, $^{87}Rb_2$ and $^{85}Rb^{87}Rb$) in their natural abundances, and the final judgment upon agreement of the calculation and the experiment can be made after examination of their influence on the spectrum. In the following we will take a closer look on the parameters, which can influence the spectral simulations: the strength of the spin-orbit coupling and the kind of the isotopomer.

The simplest way to look at the effect of the spin-orbit coupling on the *A* and *b* states is to compute the rotational constants with the FGH method for Hund's case (a) (B_v^A and B_v^b), Hund's case (c) (B_v^{lower} and B_v^{upper} for the lower and upper 0_u^+ state, respectively), and in the coupled *A-b* system. The results are displayed in Fig. 9 for $^{85}Rb_2$ isotopomer with two choices of the spin-orbit coupling. The case of *R*-independent coupling (proportional to the atomic fine
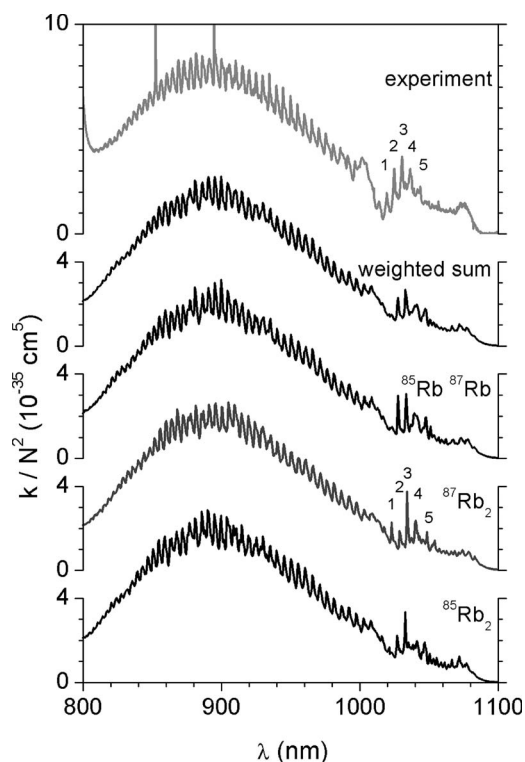
FIG. 11. The reduced absorption coefficient of the Rb_2 X-A band calculated ($T^{fit}=620$ K) for different isotopomers with variable spin-orbit coupling and compared with the experimental spectrum ($T^{expt}=615$ K).

structure splitting ΔE_{FS}) is depicted in Fig. 9(a). Figure 9(b) shows the result obtained for R-dependent coupling, introduced through $W_{SO}^d(R)$ and $W_{SO}^{o-d}(R)$ in Eq. (8) in place of ΔE_{FS} in diagonal and off-diagonal matrix elements, respectively. The value of $W_{SO}(R)$ was obtained by scaling calculated coupling in K_2 [15] to the asymptotic coupling of Rb_2. We also tried the scaling of the computed Cs_2 coupling as in Ref. [10], but the results were slightly less satisfactory. As expected for the single state cases (i) and (ii), the rotational constant has a smooth variation with binding energy. The "noisy" variation in case (iii) reflects that the system is neither described by pure Hund's case (a) nor Hund's case (c). Regarding the influence of the spin-orbit coupling, it can be seen that the rotational constants in the coupled A-b system [Fig. 9(b)] are somewhat closer to the Hund's case-(a) situation, when compared with the results obtained for constant spin-orbit coupling [Fig. 9(a)]. As suggested by Eq. (4) the values of the rotational constants B_v influence the amplitude of the modulation as can be clearly seen in Fig. 8.

We have also examined the influence of the different isotopomers ($^{85}Rb_2$, $^{87}Rb_2$ and $^{85}Rb^{87}Rb$) on the results for the rotational constants and consequently the simulation of the reduced absorption coefficient. The results obtained using the R-dependent spin-orbit coupling are shown in Fig. 10. As the A-b mixing results in a resonant coupling between vibrational levels from each state, the mass of the considered species induces different resonance conditions, and then modifies the variations of the rotational constants. The spectrum is found very sensitive to the isotope (Fig. 11): the relative
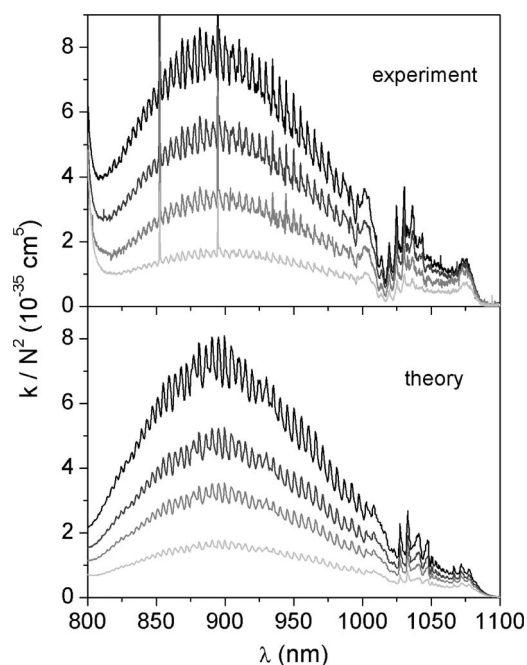
FIG. 12. The comparison of simulated and measured reduced absorption coefficients in the Rb_2 X-A band for four different temperatures given in Fig. 5. Quantum mechanical simulations were performed with R-dependent spin-orbit coupling and taking into account the weighted sum of different isotopomer contributions.

intensities of the peaks (labeled with 1–5 in Fig. 11) around 1020 nm vary significantly for different isotopomers. When adding the contributions from three isotopomers weighted by their natural abundance (as it is the case in the experiment), the agreement of the simulation with the experimental signal is found to be satisfactory.

The analysis performed shows that the simulated reduced absorption coefficient in X-A band strongly depends on the chosen parameters (strength of spin-orbit coupling, kind of the isotopomer). Cases (i) and (ii) are clearly unable to reproduce the experimental spectra satisfactorily. The agreement improves in the coupled state picture, as the simulation now involves the possible resonances between vibrational levels. We reported in Fig. 12 the simulations for the four different temperatures, compared to the experimental signal. It can be seen that with R-dependent spin-orbit coupling and inclusion of the contributions arising from all isotopomers the experimental results are reproduced correctly.

V. CONCLUSION

Theoretical and experimental investigations of the atomic and molecular features appearing between 600 and 1100 nm in the absorption spectrum of the rubidium dimer have been presented. The temperature range covered by calculations and measurements extended from 615 to 745 K. The interaction potentials and the corresponding dipole moments of all transitions contributing to the considered absorption spectrum were used as an input for the performed semiclassical and quantum mechanical simulations. Apart from the potentials of $1\,^1\Sigma_g^+$ and $1\,^1\Pi_u$ states, which were available in lit-

erature [5,6], all other required potentials and transition dipole moments were calculated in the present work. The semiclassical approach was found to reproduce well the gross spectral features. To reproduce the oscillatory behavior of the reduced absorption coefficient in the *X-B* and *X-A* bands it was necessary to treat the bound-bound contributions to the spectrum within quantum mechanical formalism. The *X-A* band has been investigated in more detail by applying three different frameworks (Hund's case (a), Hund's case (c), and two coupled channels) and it was shown that the two coupled channel approach provides the best insight into the mechanism of the formation of *X-A* band. The oscillatory behavior of the absorption coefficient in the *X-A* was found to reflect the energy dependence of the rotational B_v constants. The used vibrational band continuum approximation combined with the Fourier grid Hamiltonian method provided good reproduction of important quantum mechanical features, suggesting that this relatively simple and reliable method could be equally applied to other homonuclear or heteronuclear heavy alkali-metal systems. Also, it was shown

that the inclusion of *R*-dependent spin-orbit coupling and the contributions from all isotopomers substantially improved the agreement with the experiment. The reduced absorption coefficient has been experimentally determined by white-light absorption measurements in an overheated rubidium vapor with radial temperature gradient. Spatially resolved measurements enabled almost simultaneous measurements at a series of different temperatures under the same steady state conditions. Good agreement was found between the theoretical and experimental spectra with respect to positions and relative intensities of the molecular features, which includes the modulations in the absorption coefficient observed in *X-A* band.

ACKNOWLEDGMENTS

[1] H.-K. Chung, K. Kirby, and J. F. Babb, Phys. Rev. A **60**, 2002 (1999).

[2] H.-K. Chung, K. Kirby, and J. F. Babb, Phys. Rev. A **63**, 032516 (2001).

[3] C. Vadla, R. Beuc, V. Horvatic, M. Movre, A. Quentmeier, and K. Niemax, Eur. Phys. J. D **37**, 37 (2006).

[4] C. Amiot, J. Chem. Phys. **93**, 8591 (1990).

[5] J. Y. Seto, R. J. Le Roy, J. Vergès, and C. Amiot, J. Chem. Phys. **113**, 3067 (2000); note that the photoassociation spectroscopic analysis of Tsai *et al.* [Phys. Rev. Lett. **79**, 1245 (1997)] gives $D_e = 3993.53(6)$ cm^{-1}.

[6] C. Amiot and J. Vergès, Chem. Phys. Lett. **274**, 91 (1997).

[7] D. L. Drummond and L. A. Schlie, J. Chem. Phys. **65**, 2116 (1976).

[8] C. Amiot, O. Dulieu, and J. Vergès, Phys. Rev. Lett. **83**, 2316 (1999).

[9] V. Kokoouline, O. Dulieu, R. Kosloff, and F. Masnou-Seeuws, J. Chem. Phys. **110**, 9865 (1999).

[10] V. Kokoouline, O. Dulieu, and F. Masnou-Seeuws, Phys. Rev. A **62**, 022504 (2000).

[11] C. Lisdat, O. Dulieu, H. Knöckel, and E. Tiemann, Eur. Phys. J. D **17**, 319 (2001).

[12] G. V. Pitatelev and V. I. Lukashenko, Opt. Commun. **55**, 110 (1985).

[13] J. Lozeille, A. Fioretti, C. Gabbanini, Y. Huang, H. K. Pechkis, D. Wang, P. L. Gould, E. E. Eyler, W. C. Stwalley, M. Aymar, and O. Dulieu, Eur. Phys. J. D **39**, 261 (2006).

[14] Y. Lee, Y. Yoon, S. J. Baek, D.-L. Joo, J.-s. Ryu, and B. Kim, J. Chem. Phys. **113**, 2116 (2000).

[15] M. Foucrault, Ph. Millié, and J. P. Daudey, J. Chem. Phys. **96**, 1257 (1992).

[16] S. J. Park, S. W. Suh, Y. S. Lee, and G.-H. Jeung, J. Mol. Spectrosc. **207**, 129 (2001).

[17] D. Edvardsson, S. Lunell, and Ch. M. Marian, Mol. Phys. **101**, 2381 (2003).

[18] N. Gador, B. Zhang, H. O. Karlsson, and T. Hansson, Phys. Rev. A **70**, 033418 (2004).

[19] M. Aymar and O. Dulieu, J. Chem. Phys. **122**, 204302 (2005).

[20] M. Aymar, O. Dulieu, and F. Spiegelmann, J. Phys. B **39**, S905 (2006).

[21] L. K. Lam, A. Gallagher, and M. M. Hessel, J. Chem. Phys. **66**, 3550 (1977).

[22] R. Beuc and V. Horvatic, J. Phys. B **25**, 1497 (1992).

[23] M. Movre and G. Pichler, J. Phys. B **13**, 697 (1980).

[24] C. C. Marston and G. G. Balint-Kurti, J. Chem. Phys. **91**, 3571 (1989).

[25] M. Marinescu and A. Dalgarno, Phys. Rev. A **52**, 311 (1995).

[26] B. Huron, J.-P. Malrieu, and P. Rancurel, J. Chem. Phys. **58**, 5745 (1973).

[27] P. Durand and J. C. Barthelat, Theor. Chim. Acta **38**, 283 (1975).

[28] M. Foucrault, Ph. Millié, and J. P. Daudey, J. Chem. Phys. **96**, 1257 (1992).

[29] See EPAPS Document No. E-PLRAAN-75-080703 for Rb$_2$ transition dipole moments. For more information on EPAPS, see http://www.aip.org/pubservs/epaps.html.

[30] O. Docenko, M. Tamanis, R. Ferber, A. Pashov, H. Knöckel, and E. Tiemann, Phys. Rev. A **69**, 042503 (2004).

[31] V. Horvatic, R. Beuc, M. Movre, and C. Vadla, J. Phys. B **26**, 3679 (1993).

[32] A. N. Nesmeyanov, in *Vapor Pressure of the Chemical Elements*, edited by R. Gray (Elsevier, Amsterdam, 1963).

[33] M. Ya. Ovchinnikova, Theor. Exp. Chem. **1**, 22 (1965).

[34] D. Aumiler, T. Ban, R. Beuc, and G. Pichler, Appl. Phys. B: Lasers Opt. **76**, 859 (2003).